A fully resolved numerical simulation of turbulent flow past one or several spherical particles

L. Botto[a] and A. Prosperetti[b]
Department of Mechanical Engineering, Johns Hopkins University, Baltimore, Maryland 21218, USA

(Received 13 September 2011; accepted 14 December 2011; published online 31 January 2012)

The flow past one or nine spheres arranged in a plane lattice held fixed in a stream of decaying homogeneous isotropic turbulence is studied by means of fully resolved Navier-Stokes simulations. The particle radius is 3–5 times the Kolmogorov length and about 1/3 of the integral length scale. The mean particle Reynolds number is 80 and the turbulence intensity 17% and 33%. Several features of the flow are described: the mean and fluctuating dissipation and its spatial distribution, the mean and fluctuating hydrodynamic forces on the spheres, stimulated vortex shedding, and others. A special attention is paid to the relation between the work done on the fluid by the particles (in the reference frame of the former) and the total dissipation. It is shown that these quantities, which are assumed to balance in many point-particle models, can actually be very different when inertial effects are important. © *2012 American Institute of Physics*. [doi:10.1063/1.3678336]

I. INTRODUCTION

Solid particles suspended in a turbulent flow can affect major features of the fluid motion such as the turbulent kinetic energy, the dissipation rate, and the energy spectrum. This turbulence modulation can be substantial. For instance, Hwang and Eaton[1] measured turbulent suppression of about 35%–40% in a particle-laden turbulent flow at particle volume fraction as small as 10^{-4} for a mass loading of about 0.3. A full understanding of this and other phenomena encountered in turbulent disperse two-phase flows is still lacking.

The vast majority of theoretical studies rely on point-particle models which are only applicable to particles smaller than the Kolmogorov scale at very dilute concentrations.[2,3] These limitations afford significant modelling simplifications stemming from the clear separation between all turbulence scales and the particle size, the absence of direct hydrodynamic interactions (with the possible exception of collisions, see e.g., Refs. 4 and 5), the existence of simple parameterizations of the particle-fluid interaction, and others. Many situations of great practical importance, however, do not permit the restrictive approximations necessary to justify the point particle model. Examples are the transport of suspended sediments, fluidized beds, the formation and dynamics of sand dunes, and others. Even when the average particle concentration is small, clustering phenomena may cause large local increases of concentration which invalidate the dilution assumption (see e.g., Refs. 6 and 7). Furthermore, even in the dilute case, significant phenomena such as particle wakes and vortex shedding are, at best, only partially accounted for by the force parameterizations commonly used.

Given its strong limitations, it is not surprising that the point-particle model has been unable to explain major experimental results such as the greatly increased dissipation of Ref. 1 or the strong dependence of the turbulence modulation on the ratio of the particle size to the integral scale of the turbulence (see e.g., Ref. 8).

[a]Present address: Department of Chemical and Biomolecular Engineering, University of Pennsylvania, Philadelphia, Pennsylvania 19104, USA. Electronic mail: lbotto@seas.upenn.edu.
[b]Also at Faculty of Science and Technology and J. M. Burgers Centre for Fluid Dynamics, University of Twente, P.O. Box 217, 7500 AE Enschede, The Netherlands. Electronic mail: prosperetti@jhu.edu.

A particularly significant aspect incompletely captured by the standard point-particle approach is the particle-induced dissipation $\mathcal{D}_p$, which is usually computed from

$$\mathcal{D}_p = \sum_{\alpha=1}^{N_p} \mathbf{F}^\alpha \cdot [\mathbf{w}^\alpha - \mathbf{u}(\mathbf{x}^\alpha, t)], \tag{1}$$

in which the sum runs over all the N_p particles. Here, $\mathbf{F}^\alpha$ is the hydrodynamic force on the αth particle, $\mathbf{w}^\alpha$ the particle velocity, and $\mathbf{u}(\mathbf{x}^\alpha, t)$ the fluid velocity at the location $\mathbf{x}^\alpha(t)$ of the particle. While this expression may approximate the work per unit time done by very small particles on the fluid (in the local frame of reference of the fluid), it must be recognized that not all of this work is dissipated in the neighborhood of the particle. In part, it will increase the kinetic energy of the fluid and will be dissipated only later and farther away from the particle. This process occurs jointly with the single-phase turbulence energy cascade and it is by no means clear how to separate the two dissipative mechanisms.[9] The increased fluid kinetic energy can also interact with downstream particles affecting their wake and, among others, modulating the shedding of vorticity, all of which are effects which cannot be captured by the simple superposition hypothesis on which Eq. (1) rests. These phenomena acquire a much greater prominence when the particle size is not small compared with at least some of the flow scales. This is the situation considered in the present paper.

We report results of direct numerical simulations of turbulent flow with a mean velocity U past one or several fixed spheres at a single Reynolds number $Re_p = 2aU/\nu = 80$, with a the particle radius and ν the fluid kinematic viscosity. The turbulence is generated in a computational domain devoid of particles and convected over the particles as it freely decays. We consider two cases with incident turbulence intensities corresponding to Taylor microscale Reynolds numbers $Re_\lambda = 17$ and 24. These relatively small values of Re_λ are typical of flows in which turbulence is produced by the particles themselves.[10] The spatial extent of the spheres is fully resolved and the ratio of their radius to the Kolmogorov scale is 3.4 and 5.4 in the two cases.

The computational challenge that needs to be faced in the attempt to go beyond the point-particle model is substantial. The surface of each particle must be recognized as an internal boundary of the flow and the discretization must be fine enough to permit the imposition of the no-slip condition and an accurate determination of the force and couple on each particle. Not surprisingly, therefore, there is only a limited number of studies which have attempted the simulation of finite-size particles in a turbulent flow and, in all of them, the total number of particles considered is many orders of magnitude smaller than what is possible with the point particle model.

Numerical simulations of a single stationary sphere in decaying isotropic turbulence have been reported in Refs. 9 and 11 for particle radii about 1 and 4 times the Kolmogorov length scale, respectively; the Reynolds number based on the rms velocity fluctuation and the particle diameter was close to 20 in both cases. Both studies found a substantially higher dissipation in the presence of the particle compared with the particle-free case, mostly originating in a boundary-layer-like region very near the particle surface, but also extending as far as one radius from the particle.

In the presence of a mean flow, a wake develops and the dissipation fields become strongly anisotropic. This situation has been studied in an early pioneering work by Yusof[12] and, in greater detail, by Bagchi and Balachandar[13] who focused in particular on the wake structure and the turbulent kinetic energy distribution at Reynolds numbers between 60 and 600 and turbulence intensities between 9% and 26%. Their results at low turbulence intensities were in good agreement with the early experiments of Faeth and Wu,[14,15] who studied various features of the flow past a stationary sphere in a similar Reynolds number range at relatively low turbulence intensities of a few percent.

The present study is similar to that of Bagchi and Balachandar,[13] the main difference lying in the Taylor microscale Reynolds number which was 164 in their work and, therefore, much larger than here. For isotropic homogeneous turbulence, the ratio of the integral length scale ℓ to the particle diameter can be estimated to be[16]

$$\frac{\ell}{2a} \simeq \frac{1}{10} \frac{Re_\lambda^2}{(u'/U) Re_p}. \tag{2}$$

Therefore, for comparable Re_p and turbulence intensity, a larger Re_λ translates into a much larger integral scale. With our parameter values, the integral length scale is only a few times larger than the particle diameter and the particle-turbulence interaction, therefore, very different from that studied in Ref. 13. The values of Re_λ we simulate are comparable to the smallest one in the experiments of Ref. 10, in which a single sphere was exposed to a turbulent stream, which was $Re_\lambda \simeq 35$. Since the smallest particle Reynolds number considered in this study was 110, and, therefore, only slightly larger than ours, we can effect some comparisons of our results with these recent measurements.

As already noted, our principal focus is the nature and spatial distribution of the energy dissipation in the presence of a mean flow, which has remained a largely unexplored topic. The substantial body of work done on the turbulent wake dissipation at high particle Reynolds number (see e.g., Ref. 17) is not relevant for the relatively low Reynolds numbers occurring in typical disperse particle flows. For example, in both sprays and fluidized beds, typical particle Reynolds numbers are of the order of 100.[18,19]

Admittedly fixed particles are a very special situation. Nevertheless, a fundamental understanding of the basic physics in this simple case can help shed some light on the results of larger-scale experiments or computations such as those reported in Refs. 20–22.

II. NUMERICAL METHOD

The simulations were carried out with the *Physalis* method, details of which can be found in Refs. 23–25. Briefly, this is an immersed-boundary method which differs from the more standard ones in that the boundary conditions on the particle surfaces are imposed with the aid of a local spectral representation of the solution. This representation is based on the observation that, due to the no-slip condition, the fluid velocity very near the particle is only slightly different from a solid-body motion. The Navier-Stokes equations can, therefore, be linearized and, after a change of the dependent variables, formally reduced to the linear Stokes equations. Lamb's general solution for flow around a sphere[26,27] can then be used in this thin region adjacent to the particle surface (which is referred to as the "cage") to construct a spectral representation of the flow variables in terms of undetermined coefficients. The final solution is then found by matching the local solution to a finite-difference one valid outside the particle cages, based on a staggered, finite-difference uniform grid. Time advancement proceeds by a standard second-order projection method.

A major advantage of this approach with respect to other immersed-boundary methods is that the local solution, being spectral in nature, permits an accurate representation of the flow by means of a relatively small number of parameters, namely the coefficients of the local solution. As this number is increased, the error decreases spectrally rather than algebraically as in conventional methods. Furthermore, the no-slip condition is enforced exactly and the hydrodynamic force and couple on the particle are obtained directly rather than by integrating the stress over the particle surface as they are the low-order coefficients of the local analytic solution.

The *Physalis* method has been extensively validated with excellent results by comparison with analytical solutions, standard drag correlations, and experiments.[23,25,28,29] A recent application to a homogeneous turbulent flow with no mean velocity around a fixed sphere has been described in Ref. 11. Results for the unsteady sedimentation of 1024 spheres[28] suggest that reasonably accurate results can also be obtained in strongly non-uniform flows involving many particles. Further comments on the validation of the method for the present application are given in Sec. III.

A distinct feature of the present implementation of the method with respect to earlier ones is the use of a specialized multigrid algorithm which greatly facilitates the solution of the pressure Poisson equation. Details of the method are given in Ref. 30 and will be subject to a forthcoming publication. By having recourse to this strategy, it was possible to carry out the present simulations on a single processor.

III. OVERVIEW OF THE SIMULATIONS

The simulations were carried out using two computational domains, $\mathcal{A}$ and $\mathcal{B}$ (Figure 1), the latter one containing one or more spheres of radius a arranged on the plane $x = 0$ (Figure 2).

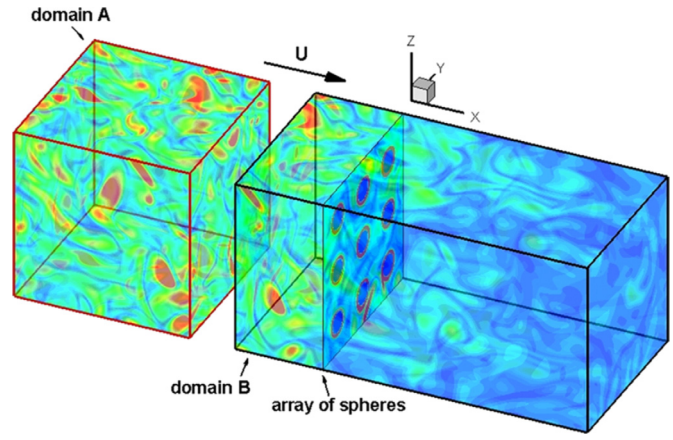

FIG. 1. (Color online) Schematic of the simulation set-up. A homogeneous isotropic turbulent field $\mathbf{u}'$ generated in the domain $\mathcal{A}$ is convected with a mean velocity $\mathbf{U}$ past the spheres held fixed in the domain $\mathcal{B}$. The x-axis is directed downstream, with $x = -8a$ corresponding to the inflow plane of the domain $\mathcal{B}$; y and z are the cross-stream coordinates.

Domain $\mathcal{A}$ was a cube with side $L = 16a$, while domain $\mathcal{B}$ had dimensions $2L \times L \times L$ in the (x, y, z) directions, respectively.

Homogeneous, isotropic turbulence was generated in domain $\mathcal{A}$ using the linear forcing of Lundgren[31,32] with periodic boundary conditions in all directions. It is known that, with this scheme, the integral length scale of the turbulence is approximately equal to $0.19L$ (Refs. 31 and 32) and, therefore, in this case, about $3a$. The initial condition was a solenoidal velocity field with a given turbulent energy spectrum.[11] The simulations were considered statistically stationary when the short-time average of the fluctuating force on each particle became essentially constant.

Let (x', y', z') and (x, y, z) denote the coordinates in the domains $\mathcal{A}$ and $\mathcal{B}$, respectively (Figure 1). The axes x and x' are parallel and oriented in the direction of the mean flow, with $x' = 0$ denoting the left boundary of domain $\mathcal{A}$ and $x = -8a$ that of domain $\mathcal{B}$. The turbulent velocity field $\mathbf{u}'$ on a plane moving from right to left into domain $\mathcal{A}$ at a constant velocity $-\mathbf{U} = U\mathbf{e}_{x'}$ parallel to the x'-axis is used as the inflow condition for domain $\mathcal{B}$ which contains the sphere(s). Specifically, the inlet boundary condition for domain $\mathcal{B}$ is taken as

$$\mathbf{u}(x = -8a, y, z, t) = \mathbf{U} + \mathbf{u}'(L - Ut, y = y', z = z', t). \tag{3}$$

Here, the variable $L - Ut$ must be understood modulo L/U, so that the plane starts traversing the domain $\mathcal{A}$ again from right to left every time it reaches the left boundary.

The procedure just described effectively enables us to model one or several spheres translating without rotation with velocity $\mathbf{U}$ in a time-dependent, homogeneous, freely evolving isotropic turbulent field. An essential difference with the earlier work described in Ref. 12 and the subsequent one of Refs. 13 and 33 is that these authors convected a frozen velocity field past the

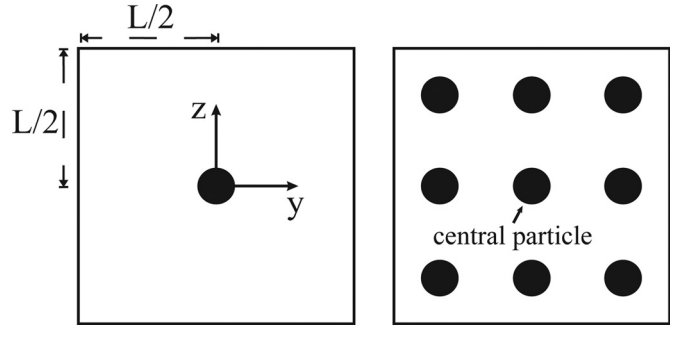

FIG. 2. Particle arrangements for the single particle (left) and multi-particle simulations. The side of the square is 16 times the particle radius. The area fraction occupied by the particles is 1.23% and 11.0%.

particle. The extent L of the domain in which the turbulent flow was generated needed therefore to be so large that the duration L/U of the simulation was sufficient to permit the computation of representative time averages. In our simulations, the same objective is attained with a smaller domain by allowing the turbulence generated in the domain $\mathcal{A}$ to freely evolve in time for the duration of the entire simulation. As long as the properties of the turbulence thus generated change appreciably over the time scale L/U, the inflow is effectively non periodic. In our case, the eddy turnover time of the inflow turbulence was between 1.16 and 2.6 times smaller than L/U so that the correlation between successive traverses may be expected to be relatively small.

While numerically efficient, the present setup has the shortcoming that the spacing between the real (and also the image) particles is connected to the integral length scale of the turbulence which is determined by the cross-stream dimension of the domain as noted before. A change in the particle spacing would, therefore, affect the character of the incident turbulence.

The convective outflow condition $\partial\mathbf{u}/\partial x = 0$ was applied at the downstream boundary of $\mathcal{B}$ and periodicity conditions on all the lateral boundaries.

A useful feature of the use of two separate domains is that exactly the same inflow condition can be used for one, several, or no particles in domain $\mathcal{B}$ provided care is taken to update the flow in domain $\mathcal{A}$ using precisely the same sequence of time steps. In particular, we have made use of this possibility to carry out particle-free simulations in domain $\mathcal{B}$ to serve as reference.

We have considered two particle arrangements (Figure 2), one with a single sphere and one with nine spheres arranged in a square lattice located on the plane $x = 0$ normal to the inflow direction 8 radii downstream of the inflow boundary (Figure 1). The solidity, or area fraction, occupied by the spheres was 1.23% and 11.0% in the two cases. If the incident flow were laminar, in view of the periodicity conditions on the lateral boundaries, we would be effectively simulating the flow past infinite planar arrays of particles of different solidity. The turbulent nature of the incident flow makes this argument applicable only in a statistical sense.

The turbulence intensities in the particle-free domain $\mathcal{A}$, calculated on the basis of the rms velocity fluctuations u', were $u'/U = 22\%$ and 49%, with eddy turnover times of $13.72a/U$ and $6.08a/U$ and corresponding values of $Re_\lambda = \lambda u'/\nu \simeq 20$ and 33. The turbulence decays as it is convected into the particle domain $\mathcal{B}$. The rms velocity fluctuation u' at the position occupied by the center of the (central) particle in the absence of the particle, obtained from separate particle-free simulations, was $u'/U = 17\%$ and $u'/U = 33\%$ in the two cases. Each simulation was run for 60 eddy turnover times after statistical stationarity was achieved. If each eddy turnover time can be considered as an independent realization of the flow, the statistical error can be estimated to be about $1/\sqrt{60} \simeq 13\%$.

All the simulations were carried out for a particle Reynolds number $Re_p = 2U\,a/\nu = 80$, which is representative of the range encountered in several experiments[34–37] and applications. At this Reynolds number, a sphere wake is well developed, steady, and axisymmetric in the absence of turbulence.[38]

We checked that the features of the turbulence generated in domain $\mathcal{A}$, and in particular intensity and integral length scales, matched the results reported in Ref. 32. The main parameters of the simulations, including the Kolmogorov and the integral length scales η and ℓ, are summarized in Table I. It can be seen here that the particles are larger than the Kolmogorov scale and of the same order as the Taylor microscale.

TABLE I. Characteristics of the homogeneous isotropic turbulence generated in the domain $\mathcal{A}$ and on the plane $x = 0$ in the domain B: u'/U: turbulence intensity; Re_λ: Taylor-microscale turbulence Reynolds number; η: Kolmogorov scale; λ: Taylor micro-scale; and $\ell = u'^3/\epsilon$: integral scale. As the turbulence is convected into the domain $\mathcal{B}$, it decays and its intensity at the position of the center of the (central) particle (in the absence of the particle) is $u'/U = 17\%$ or 33% as shown in the last column. The mean particle Reynolds number is 80.

	Domain $\mathcal{A}$					Domain $\mathcal{B}$				
No. of particles	Re_λ	a/η	λ/a	ℓ/a	u'/U	Re_λ	a/η	λ/a	ℓ/a	u'/U
1	19.7	3.8	2.3	3.0	22%	16.9	3.4	2.4	2.6	17%
1	32.7	6.8	1.6	3.6	49%	24.2	5.4	1.8	2.9	33%
9	32.7	6.8	1.6	3.6	49%	24.2	5.4	1.8	2.9	33%

Our choice of parameters represents a compromise between the need to keep the computational effort manageable, while at the same time obtaining reasonably well-resolved results, and the desire to simulate a turbulence of a sufficient level as to mitigate the effect of its decay during the time needed to convect it past the particles. Data on the rate of decay of the incident turbulence are shown later in Figures 7, 8, and 17.

The grid was uniform with a mesh $\Delta x = L/128$ in all directions for both domains $\mathcal{A}$ and $\mathcal{B}$. This translates into 16 mesh lengths per particle diameter, which is similar to the value used by other authors,[20–22] but may be expected to give an improved resolution here due to the spectral convergence of the *Physalis* expansion. The expansion was truncated keeping terms of order 0, 1, and 2, which corresponds to retaining a total of 25 coefficients. It was shown in Ref. 25 that this order of truncation and $2a/\Delta x = 16$ give very good results for the drag and the flow past a particle in a uniform incident flow with $Re = 100$. As a further check, we carried out some preliminary tests at higher resolution for the steady laminar flow past a fixed sphere at $Re = 80$. We did not find any significant difference in the location of the separation point on the sphere surface or in the length of the recirculating wake. It may also be noted that, with the present parameter values, the need to resolve a boundary layer of thickness $\delta \sim a/\sqrt{Re_p}$ is a more stringent condition than that required by resolution of the Kolmogorov scale.

To test the accuracy of the turbulent simulations, we computed the drag coefficient C_d on a single particle and compared our results with those of Ref. 33. The authors found that the mean drag coefficient for an isolated sphere in a turbulent flow was within 8% of the value given by the Schiller-Naumann correlation (see e.g., Ref. 39) evaluated at the mean particle Reynolds number defined in terms of the mean single-phase undisturbed velocity at the particle position. Using the same definitions for the mean particle Reynolds number and drag coefficient, we found $C_d = 1.11$ and 1.16 at $Re_\lambda = 20$ and 33 and $Re_p = 80$. These results are within 3% of the value given by the Schiller-Naumann correlation.

The data on the viscous dissipation shown below were computed from the numerical simulations with second-order accuracy in space. The standard central difference formula was used for all the nodes more than one mesh length away from the particle surface. At other nodes a one-sided, second-order approximation involving only fluid nodes was used.

IV. DISSIPATION

At a fixed position, the instantaneous viscous dissipation per unit mass is given in terms of the kinematic viscosity ν and strain rate tensor S_{ij} by

$$\epsilon = 2\nu S_{ij} S_{ij}. \tag{4}$$

Near the particle, the order of magnitude of S_{ij} can be estimated as U/δ, with $a/\delta = \sqrt{Ua/\nu}$, so that a suitable scale for ϵ is given by the quantity

$$\epsilon_s = \nu U^2 \left(\frac{1}{a} \sqrt{\frac{Ua}{\nu}} \right)^2 = \frac{U^3}{a}. \tag{5}$$

In the following, we present results for $\epsilon_* = \epsilon/\epsilon_s = a\epsilon/U^3$. This quantity will be of order 1 only near the particle; farther away one may expect to encounter much smaller values.

The local dissipation ϵ_* can be decomposed into a component $\bar{\epsilon}_*$ due to the time-averaged flow

$$\bar{\epsilon}_* = 2\nu \frac{\langle S_{ij} \rangle \langle S_{ij} \rangle}{\epsilon_s}, \tag{6}$$

and a component ϵ'_* due to the fluctuating flow

$$\epsilon'_* = \epsilon_* - \bar{\epsilon}_*. \tag{7}$$

In this paper, we consistently use angle brackets to denote time-mean values, but we have written here $\bar{\epsilon}_*$ because, clearly, $\langle \epsilon_* \rangle \neq \bar{\epsilon}_*$.

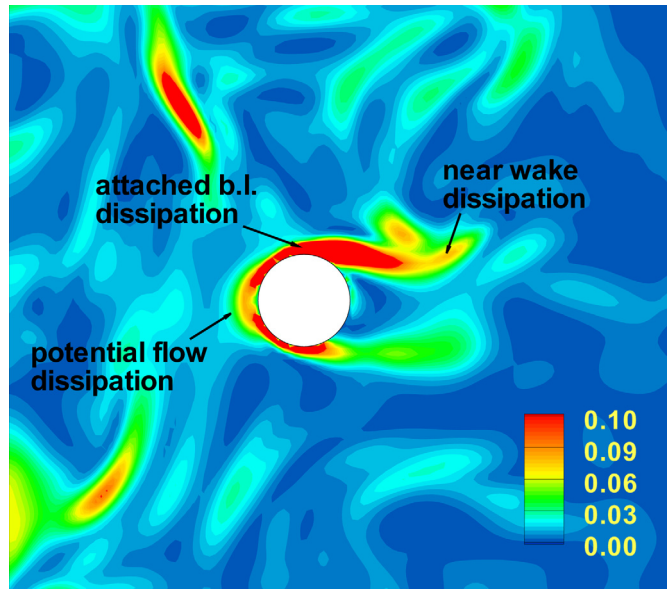

FIG. 3. (Color online) A snapshot of the normalized total instantaneous dissipation $a\epsilon/U^3$ for $u'/U = 33\%$.

V. RESULTS: SINGLE-PARTICLE SIMULATIONS

In this section we consider the effect of the incident turbulence intensity u'/U on the values of $\bar{\epsilon}_*$ and ϵ'_* for a single particle. To quantify the contribution of the particle to the flow statistics, we compare $\bar{\epsilon}_*$ and ϵ'_* to the similarly normalized fluctuating dissipation ϵ'_0 from separate calculations with no particles in the domain $\mathcal{B}$.

An instantaneous view of the distribution of the normalized dissipation ϵ_* for $u'/U = 33\%$ is provided in Figure 3 where the boundary layer, potential flow, and separated flow regions are also identified.

A. Mean flow

Earlier work has shown that, for small turbulence intensities, the mean velocity defect in an intermediate region of the sphere wake (downstream of the near wake) decreases proportionally to a/x (see e.g., Refs. 13–15 and 40) while, at higher turbulence intensities, it decays proportionally to $(a/x)^2$ (see Refs. 10 and 40). Figure 4 shows our results for this quantity for the two incident turbulent intensities with the slopes a/x and $(a/x)^2$ indicated by the thin dashed lines. The results for $u'/U = 33\%$ exhibit a clear intermediate region of proportionality to $(a/x)^2$. By the time the final

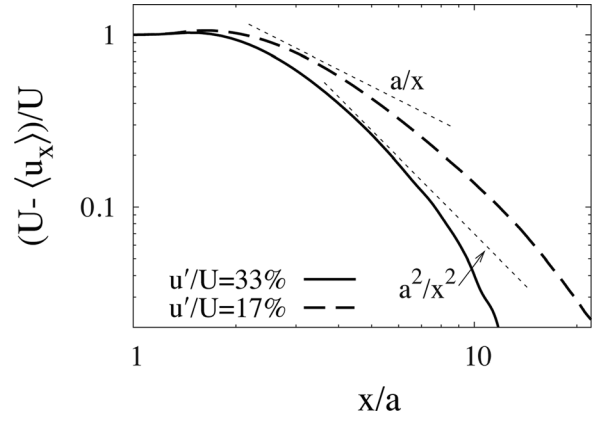

FIG. 4. Mean velocity defect along the mean wake symmetry axis behind a particle in an incident turbulent flow for two turbulence intensities. The straight lines indicate decays proportional to the inverse and inverse square of the distance.

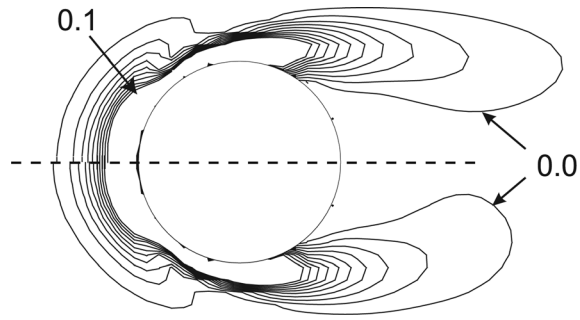

FIG. 5. Iso-contours of normalized mean-flow dissipation $a\bar{\epsilon}/U^3$ for turbulent flow past a single particle. Top half: $u'/U = 17\%$ and bottom half: $u'/U = 33\%$.

decay region is reached, turbulence has been considerably dampened and the decay is faster. For $u'/U = 17\%$, the turbulence intensity is never large enough to exhibit the inverse square law decay. However, a proportionality to a/x in the intermediate region is perhaps discernible. These trends are suggestive of what might be expected if the incident turbulence maintained a uniform intensity in the streamwise direction.

Figure 5 compares iso-contours of the local dissipation $\bar{\epsilon}_*$ due to the mean flow for $u'/U = 17\%$ (top half) and $u'/U = 33\%$ (bottom half). The iso-contours immediately adjacent the sphere surface are not shown to avoid crowding the figure.

Aside from the immediate neighborhood of the sphere surface, it can be seen that there are two distinct regions of relatively high dissipation. The first one, vaguely mushroom-shaped, is in front of the sphere, where the flow is similar to that due to a potential source (see e.g., Refs. 41 and 42). A similar feature can also be seen in Figure 15 of Ref. 9, showing the instantaneous distribution of dissipation for a fixed particle in decaying turbulence in the absence of mean flow. The other region of high dissipation is associated with the separated flow. The contours in the lower part of the figure, corresponding to the higher-turbulence case, are somewhat shorter than those for lower turbulence because the stronger disturbance of the wake decreases the mean values. This feature is in agreement with the shortening of the mean wake with increasing turbulence found in earlier studies.[13,14]

A different perspective on the same quantity, the mean-flow dissipation $\bar{\epsilon}_*$, is provided by Figure 6 which shows results for the laminar case, with $u'/U = 0$, and the two turbulent cases $u'/U = 17\%$ and 33%, along the horizontal line $z = 0$ on cross-stream planes located 3 and 9 radii downstream of the sphere center. Again one notices here a decrease of the gradients of the mean flow caused by the mixing action of the incident turbulence. With increasing turbulence level, the position of the maxima moves toward the axis of mean symmetry in agreement with Figure 5. Furthermore, the turbulent mean values decrease with distance from the sphere much more rapidly than the laminar ones. The maximum values of $\bar{\epsilon}_*$ are about 2 orders of magnitude smaller than the estimate Eq. (5) valid in the boundary layer of the sphere and are strongly reduced with

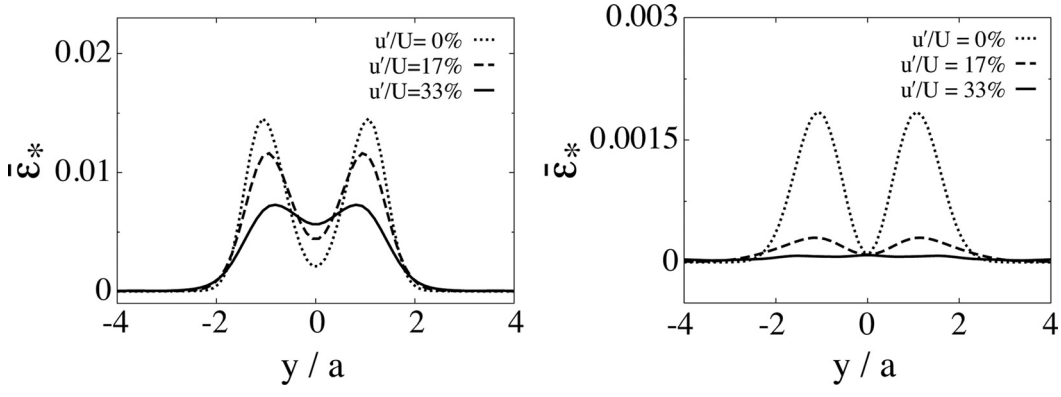

FIG. 6. Cross-stream profiles along a line $z = 0$ (cf. Figure 2) of normalized mean-flow dissipation 3 (left) and 9 radii downstream of the particle for laminar flow, $u'/U = 0$, and two different turbulence intensities.

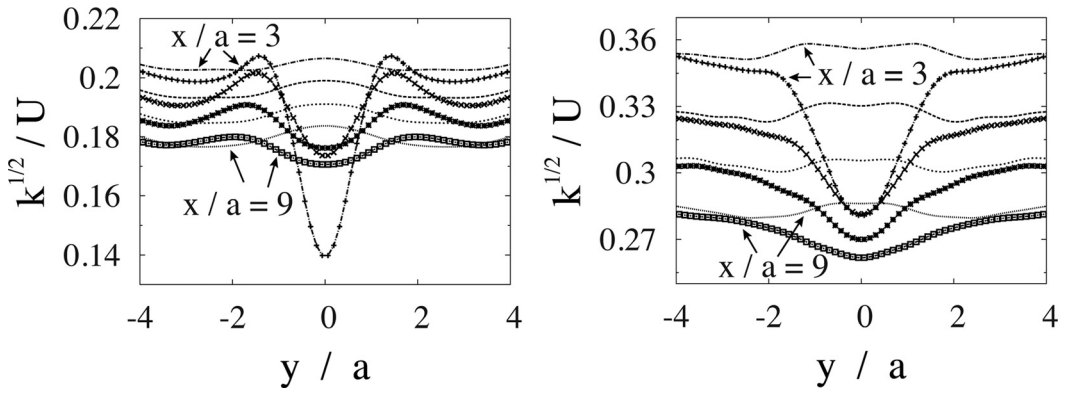

FIG. 7. Profiles of mean turbulence intensity along lines $z = 0$ on cross-stream planes 3, 5, 7, and 9 particle radii downstream of the sphere center for $u'/U = 17\%$ (left) and $u'/U = 33\%$; k is the kinetic energy of the turbulence. The thin lines are the values of k for the particle-free simulations.

increasing turbulence intensity. A comparison of the results for the two turbulence intensities illustrates the trends that can be expected in the absence of a streamwise decay of the incident turbulence. A similar consideration can be applied to the results on the statistics of the fluctuating velocity and dissipation shown below in Figures 7 and 8.

B. Fluctuations

We now turn to the fluctuating component of the dissipation defined in Eq. (7). Figure 7 shows profiles of the relative turbulence intensity $\sqrt{k}/U$, with k the turbulence kinetic energy, along lines $z = 0$ on cross-stream planes located 3, 5, 7, and 9 particle radii downstream of the sphere center. The single-phase values, obtained from separate simulations without the sphere in place, are shown by dashed lines. The small fluctuations (about 2%) about a constant value are the consequence of slightly imperfectly converged averages.

Vorticity, velocity fluctuations, and dissipation are rapidly weakened downstream of the sphere. The results with the sphere in place approach the single-phase ones outside the wake, which indicates that the domain is large enough to approximate an effectively infinite one. For the higher turbulence level (right diagram), the relative deficit of kinetic energy is smaller in agreement with the expected stronger mixing and shorter mean wake. The region of decreased velocity fluctuations, however, is significantly broadened by the stronger "flapping" of the incident stream as also found in Ref. 13.

Figure 8 compares the maximum values of the mean fluctuating dissipation $\langle \epsilon'_* \rangle$ calculated over cross-stream planes $x = \text{const.}$ (solid line), with those of the mean dissipation $\bar{\epsilon}_*$ (dotted line), as functions of the streamwise coordinate x; the dashed line is the maximum values of the particle-free dissipation over the cross-stream planes. For both turbulence intensities, the fluctuating dissipation is significantly larger than the mean one except in a relatively short region near to,

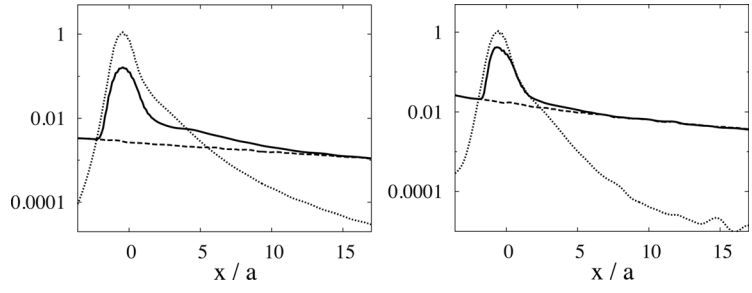

FIG. 8. The maximum values of the time-mean fluctuating dissipation rate $\langle \epsilon'_* \rangle$ (solid line) and mean dissipation rate $\bar{\epsilon}_*$ (dotted line) over cross-stream planes are shown as functions of the streamwise coordinate. The dashed line is the maximum value of the time-mean dissipation rate over cross-stream planes for the particle-free case. The left diagram is for $u'/U = 17\%$ and the right one for $u'/U = 33\%$.

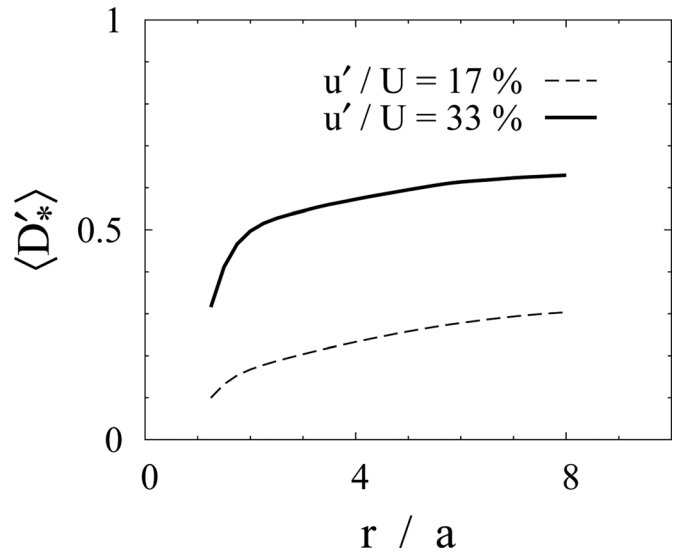

FIG. 9. Normalized integral of the mean fluctuating dissipation in excess of the particle-free case, defined in Eq. (8), over a spherical volume of radius r/a concentric with the sphere.

and mostly upstream of, the particle. Here, the strongly favorable pressure gradient causes a significant damping of the turbulent fluctuations and the dimensionless dissipation approaches 1, so that the actual mean dissipation attains the level estimated in Eq. (5). The fluctuating component matches the particle-free case at a distance of a few diameters downstream of the particle; this distance decreases with increasing incident turbulence due to the strong mixing and disruption of the wake.

While the fluctuating dissipation in the wake is much smaller than the dissipation occurring within the boundary layer, which is dominated by the mean-flow dissipation, it extends over a much larger region and the question, therefore, arises as to which of the two mechanisms contributes most to the total dissipation. To address this point we calculate the integral of $\epsilon'_* - \epsilon'_0$ (namely, the excess fluctuating dissipation over the single-phase value) over spherical shells of radius r centered at the particle as a function of r, namely, with an obvious notation,

$$\mathcal{D}'_*(r) = \frac{\mathcal{D}'}{a^2U^3} \equiv \frac{1}{a^3}\int_a^r (\epsilon'_* - \epsilon'_0)dV. \tag{8}$$

The time-mean values of this quantity are shown in Figure 9 for the two turbulent intensities. For $u'/U = 33\%$, the integral rises rapidly although it continues to grow more slowly over the entire range shown in the figure. Thus, the additional fluctuating dissipation caused by the particle contributes little to the overall dissipation beyond $r/a = 4 - 5$. For $u'/U = 17\%$, on the other hand, the particle wake is less disrupted (cf. Figures 6 and 8) and is, therefore, longer so that the integral keeps growing over a larger range. These results are consistent with those shown in Figure 8.

C. Dissipation and drag

As noted in Sec. I, it is often the case in the literature that the dissipation is estimated by equating it to the work done on the fluid per unit time by the hydrodynamic force acting on the particle. We are in a position to examine the validity of this practice.

If the conceptual picture leading to Eq. (1) is applied to the present case, the time-average of the work performed on the fluid would be given by $\langle(\mathbf{U} + \mathbf{u}'_0) \cdot \mathbf{F}\rangle$ in which $\mathbf{U} + \mathbf{u}'_0$ is the instantaneous fluid velocity at the particle center in the absence of the particle and $\mathbf{F}$ is the total hydrodynamic force on the particle. The ith component of this quantity is given by

$$F_i = -\oint p n_i dS + \rho\nu \oint S_{ij} n_j dS, \tag{9}$$

in which p is the fluid pressure and the integrals are extended over the particle surface.

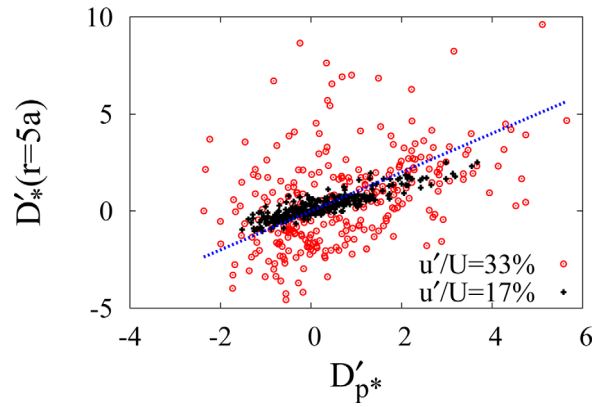

FIG. 10. (Color online) Scatter plot of the fluctuating dissipation within 2 diameters of the particle (defined in Eq. (8) with $r = 5a$) and Eq. (10)).

An integral momentum balance shows that the mean value $\mathbf{U}\cdot\langle\mathbf{F}\rangle$ equals (approximately to the extent that the integration volume is made sufficiently large, see e.g., Ref. 34) the integral of the mean-flow dissipation $\rho(\bar{\epsilon} - \bar{\epsilon}_0)$ in excess of the particle-free case. Thus, if there was a correspondence between dissipation and work, the values of the quantity

$$\mathcal{D}'_p = (\mathbf{U} + \mathbf{u}'_0)\cdot(\langle\mathbf{F}\rangle + \mathbf{F}') - \mathbf{U}\cdot\langle\mathbf{F}\rangle \tag{10}$$

should be comparable with those of the dissipation $\mathcal{D}'$ defined in Eq. (8) (see e.g., Refs. 1, 34, and 43). In an unsteady process, the difference between the two quantities is carried by the time dependence of the fluid kinetic energy.

Figure 10 shows a scatter plot of the instantaneous values of the two quantities defined in Eqs. (8) and (10); the straight line marks the locus $\mathcal{D}'_*(r = 5) = \mathcal{D}'_{p*}$, the latter quantity being nondimensionalized by division by $\rho U^3 a^2$. The dark points show the values for $u'/U = 17\%$ and the open circles those for $u'/U = 33\%$. The two quantities are reasonably close for $u'/U = 17\%$ in which case the turbulence has little energy and the unsteadiness of the flow is relatively weak. For the higher turbulence case, however, there is a large scatter in spite of the similar trend. This scatter suggests the presence of important unsteady effects which reflect small-scale processes which contribute to the dissipation but not to the force or, conversely, of large-scale flows which contribute to the force but not to the dissipation. For example, uncorrelated small-scale eddies impinging on the particle surface would contribute to the dissipation but not to the force; shed vorticity would give a contribution to the force, but it would dissipate later downstream of the particle and, therefore, not contribute to the instantaneous values of the dissipation; processes giving rise to a hydrodynamic couple on the particle would contribute to the dissipation, but not necessarily to the force.

To demonstrate the effect of non-local, far-field dissipative processes, we show in Figure 11, a scatter plot of $\mathcal{D}'_*(5a) - \mathcal{D}'_*(3a)$, namely the fluctuating dissipation in the spherical shell

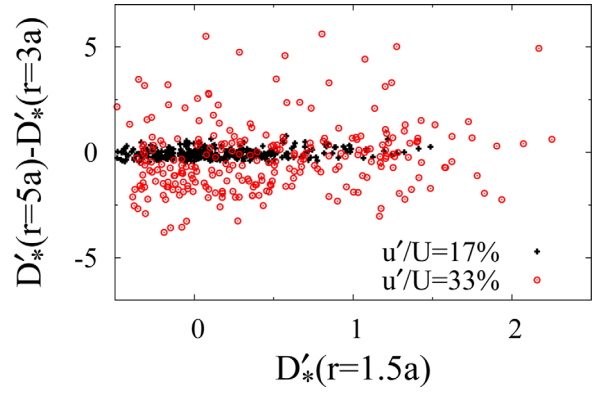

FIG. 11. (Color online) Scatter plot of the instantaneous dissipation in a fluid shell one diameter away from the particle surface vs. the instantaneous near-field dissipation within one half-radius of the particle surface.

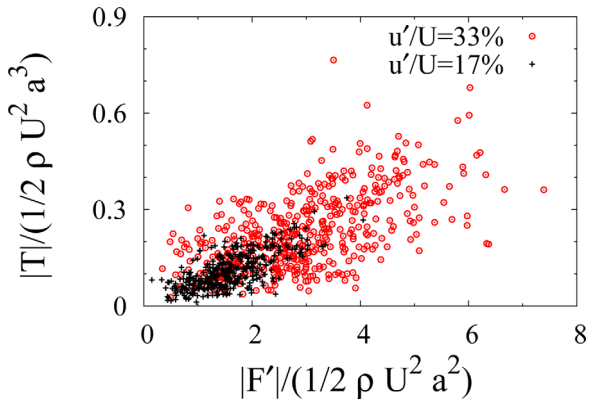

FIG. 12. (Color online) Scatter plot of the normalized instantaneous couple on the particle vs. the instantaneous force fluctuation.

between 1 and 2 diameters away from the particle, with the dissipation within 1/2 radius from the particle. It is seen that the mean value of $\mathcal{D}'_*(5a) - \mathcal{D}'_*(3a)$ is a small constant, close to zero (cf. Figure 9), while the scatter is quite substantial. We thus conclude that significant dissipative processes take place away from the particle, which have very little correlation with those near the particle. These results confirm the importance of the unsteady factors discussed in Sec. I after Eq. (1) in a situation such as the present one in which the size of the particle is not small and inertia not negligible.

It is also of interest to look at the possible correlation between the couple and the fluctuating force on the particle, which is shown in the form of a scatter plot in Figure 12 where the inner cloud of points is for $u'/U = 17\%$ and the outer one for $u'/U = 33\%$. The good correlation between the two quantities indicates that, statistically, the same processes are responsible for both of them.

D. Hydrodynamic forces

Figure 13 shows, in dimensionless form, the instantaneous value of F_x, the longitudinal component of the hydrodynamic force, and one of the transverse components, F_y, together with their decomposition in terms of pressure and viscous contributions, as functions of time. The two contributions are given, respectively, by the two terms in Eq. (9) and have been calculated as explained in Ref. 11. The time dependence of the other transverse component F_z is similar. The viscous and pressure contributions to F_x mostly have the same sign and comparable order of magnitude. The two contributions to the cross-stream component are comparable in magnitude, although on occasion their signs can be opposite. The maxima of the pressure and viscous contributions tend to occur together, although the former are larger than the latter due to the approximately quadratic dependence of the pressure on the instantaneous velocity.

It is rather remarkable that, even in the presence of a strong x-directed flow, the magnitude of the cross-stream force is not that much smaller than $\langle F_x \rangle$. This feature is due to the strong velocity fluctuations of the incident flow which cause a significant displacement of the stagnation point on the upstream side of the particle. To confirm this mechanism, we have looked at the cosine of the

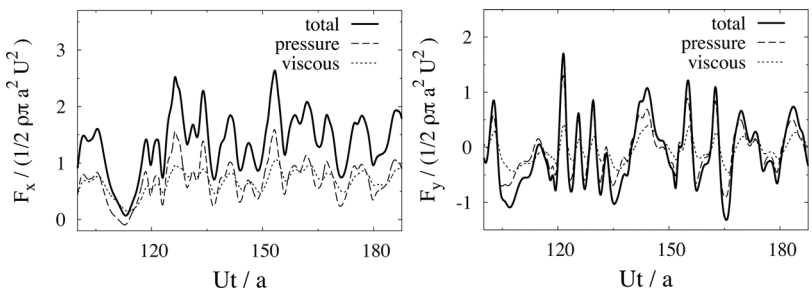

FIG. 13. Normalized forces on the particle in the x- and y-directions vs. time for $u'/U = 33\%$. The dashed and dotted lines are the pressure and viscous contributions.

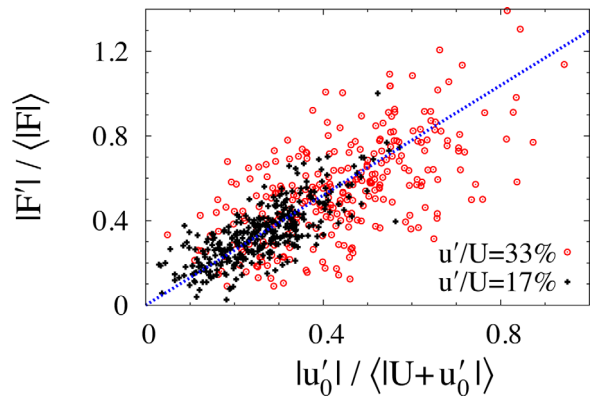

FIG. 14. (Color online) Scatter plot of the magnitude of the fluctuating force on the particle vs. the magnitude of the fluctuating velocity at the particle center in the absence of the particle.

angle between the vectors $\mathbf{F}$ and $\mathbf{U} + \mathbf{u}'_0$ and found that it is very close to 1 most of the time. The average values of this quantity for 17% and 33% are 0.99 and 0.94, respectively, with standard deviations of only 0.01 and 0.09. A further consequence of this approximate alignment is a relation of the form

$$\frac{\langle|\mathbf{F}'|\rangle}{\langle|\mathbf{F}|\rangle} \simeq C_{Fu} \frac{\langle|\mathbf{u}'_0|\rangle}{\langle|\mathbf{U} + \mathbf{u}'_0|\rangle}, \tag{11}$$

where C_{Fu} is a constant. This relation with $C_{Fu} \simeq 1.3$ is shown by the straight line in Figure 14. A linearization of the Schiller-Neumann drag relation around $Re_p = 80$ would predict a value of about 1.5 for this constant. The large scatter of the instantaneous values around this line in spite of the strong parallelism between $\mathbf{F}$ and $\mathbf{U} + \mathbf{u}'_0$ indicates the importance of unsteady force mechanisms even in the lower turbulence case.

If $\mathbf{F}'$ is isotropically distributed, $\sqrt{\frac{1}{2}(F_y'^2 + F_z'^2)} = |F_x'|$. We find $\sqrt{\frac{1}{2}(F_y'^2 + F_z'^2)}/|F_x'| = 1.08$ and 1.26 for the two turbulence intensities so that isotropy approximately prevails for the lower turbulence level, while it is violated for the higher one.

E. Other features

The computational results lend themselves to some further interesting observations. Figure 15 shows three snapshots of the normalized instantaneous dissipation ϵ_* on three cross-stream planes located 3, 4, and 5 radii downstream of the particle center; the dashed circle is the projection of the particle. In a laminar flow, there would be a tubular region of high dissipation, in correspondence with the detached boundary layer, centered around a small region of very small dissipation near the axis of the wake. The first image, closest to the sphere, shows this region of weak dissipation near the mean axis, but the surrounding high-dissipation region is dismembered by the turbulence and undergoes even greater distortions and alterations further downstream. Similar phenomena are also shown in earlier studies (see e.g., Refs. 12, 13, and 44).

An illustration of a typical mechanism of this disruption is provided in Figure 16 which shows a sequence of snapshots of the instantaneous vorticity distribution in the symmetry plane $z = 0$ parallel to the incoming flow for $u'/U = 33\%$. This sequence is taken near the beginning of the simulation as is clear by the absence of vorticity downstream of the particle in the first frame.

The first image shows two counter-rotating vortex filaments, a strong positive one labelled A and a much weaker negative one labelled B, approaching the sphere, to which two high-vorticity regions, C and D, are attached. In the second frame, the negative vortex filament B has split under the action of the stronger opposite filament just upstream of it and quickly weakens as seen in the third frame. The strong positive filament A is now close to the sphere and splits: one part merges with the attached vortex D under the sphere, while the other part interacts with the attached negative filament above the sphere and is weakened by it. The strengthened positive filament D is now too strong to remain attached (frame 5), becomes unstable, and is finally shed. While vortex

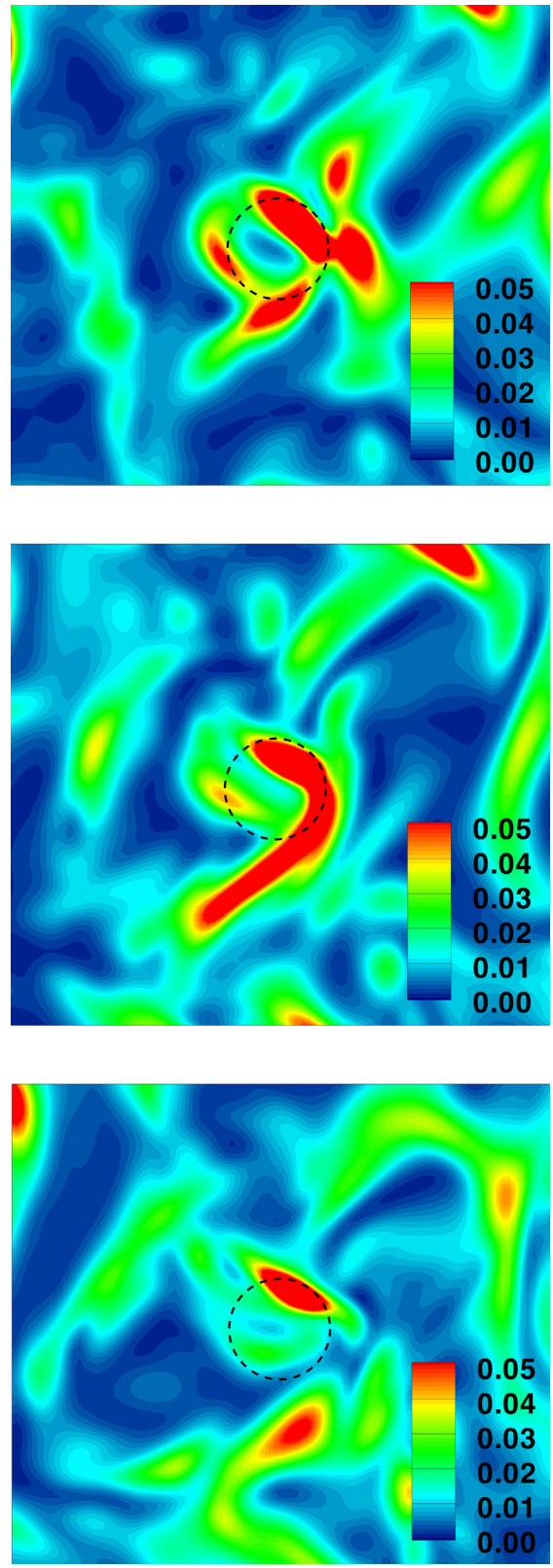

FIG. 15. (Color online) Normalized instantaneous dissipation in cross-stream planes placed 3, 4, and 5 sphere radii downstream of the sphere center for $u'/U = 33\%$; the dashed circle is the projection of the sphere.

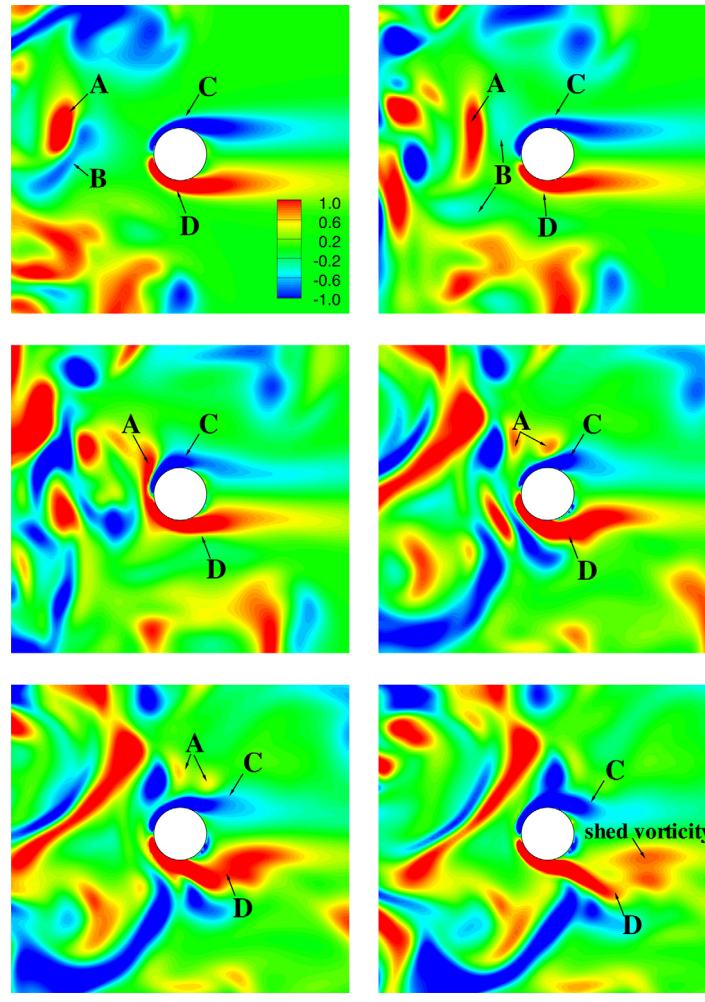

FIG. 16. (Color online) Sequence of snapshots of the instantaneous normalized vorticity $a\omega_z/U$ (positive out of the page) in the symmetry plane $z = 0$ parallel to the incoming flow for $u'/U = 33\%$. The sequence illustrates the shedding of vorticity stimulated by the impingement of free-stream turbulent vorticity. The snapshots are taken near the beginning of the simulation at times $Ut/a = 24$, 25.8, 27.8, 29.8, 30.8, and 31.8.

shedding is a well-known phenomenon, in the flow past bluff bodies, in the case of a sphere in a steady flow it is known to occur only at Reynolds numbers greater than about 270 (see e.g., Refs. 38, 45, and 46), much higher than the current value $Re_p \simeq 80$. This stimulated vortex shedding is a generic feature of flows of this type as also found by other researchers (see e.g., Ref. 13). The structure of the flow in the neighborhood of the front stagnation point remains fairly unaffected by the approaching vortex filaments, the most significant effect being a motion up and down of the stagnation point which is responsible for the fluctuating cross-stream lift force, as mentioned before. This is a generic feature that we have always observed in our simulations.

VI. RESULTS: MULTIPLE PARTICLE SIMULATIONS

We now turn to the simulations of the flow past 9 particles arranged on a plane normal to the incoming flow as in the right diagram of Figure 2. The distance between the closest points on the surface of adjacent spheres is $L/3 - 2a = (10/3)a$ and, therefore, much larger than the viscous boundary layer which has a thickness of the order of $a/\sqrt{Re} \simeq 0.11a$. Thus, there is no direct interaction between the boundary layers of adjacent spheres.

Figure 17 compares the total dissipation averaged over time and over cross-stream planes $x = \text{const.}$ normal to the incoming flow for the single- and multi-particle simulations. Downstream of the particles, the dissipation recovers the particle-free value shown by the lowest line. It must,

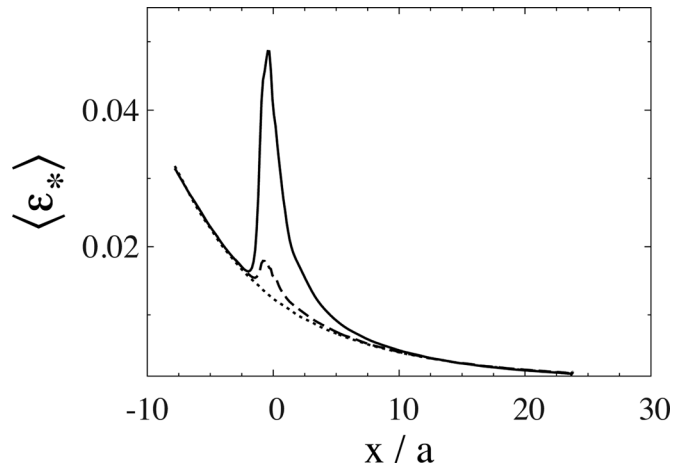

FIG. 17. Comparison between the normalized total dissipation averaged over time and over cross-stream planes $x = \text{const.}$ normal to the incoming flow for the multi- and single-particle simulations (top and middle curves, respectively). The lowest curve refers to the particle-free case. Here, $u'/U = 33\%$.

therefore, be concluded that the additional energy dissipated in the particle region is balanced by the larger pressure difference necessary to maintain the imposed velocity U. From a local point of view, the increased dissipation must be balanced by the increased production of turbulent energy caused by the stronger mean velocity gradients due to the particles. This interpretation is supported by an analysis of the Reynolds stress shown later.

The maximum of the dissipation in excess of the particle-free situation for the 9-particle case is about 11.5 times as large as the 1-particle one. In the 9-particle case, there are, therefore, additional dissipation mechanisms which do not simply scale with the particle number. The most important such mechanism is the larger boundary layer dissipation due to blockage and the consequent increased mean velocity. For a 11% solidity, the mean velocity increases from 0% just upstream of the spheres up to a maximum of about 12%. The cubic scaling shown in Eq. (5), with an average velocity increase of 8% gives an increased dissipation of 26%, in reasonable agreement with $11.5/9 \simeq 1.28$.

All the previous considerations concern local processes in the neighborhood of the particles and, therefore, may be expected to be applicable also to a situation in which the incident turbulence did not decay in the streamwise direction but remained constant.

Figure 18 compares the single- and multi-particle dissipations along the horizontal line $z = 0$ on a cross-stream plane located 3 radii downstream of the plane containing the sphere centers. The

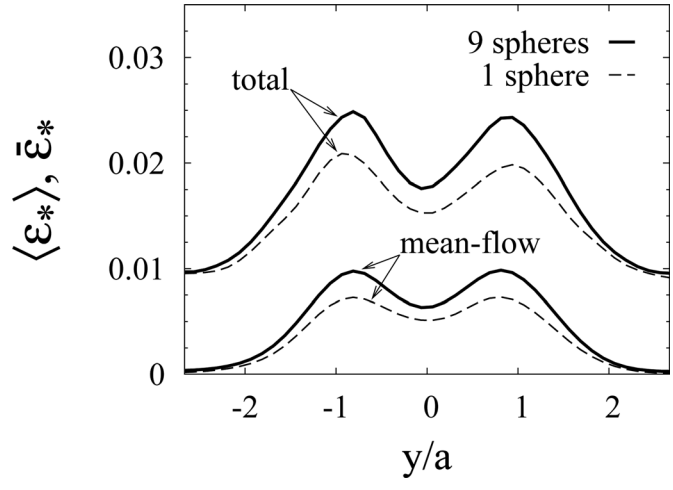

FIG. 18. Single- and multi-particle dissipation along the horizontal line $z = 0$ on a cross-stream plane located 3 radii downstream of the plane containing the sphere centers. The upper pair of curves is the total dissipation, $\langle \epsilon_* \rangle$, and the lower one that due to the mean flow, $\bar{\epsilon}_*$.

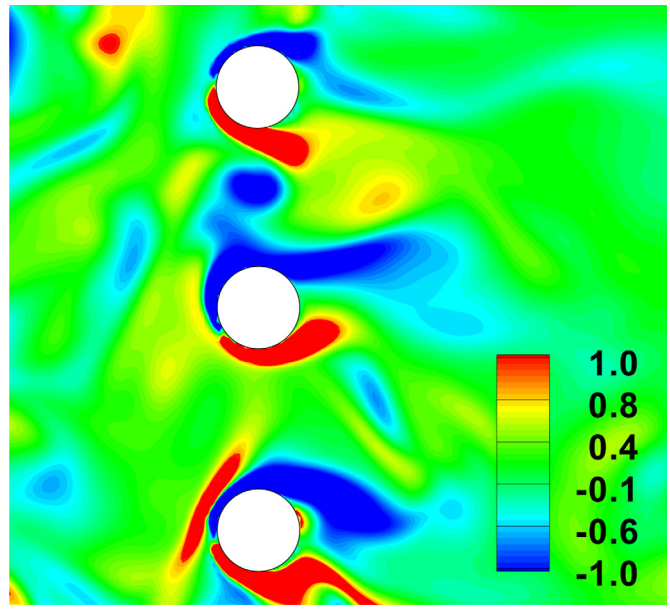

FIG. 19. (Color online) A snapshot of the instantaneous normalized vorticity component $\omega_z a/U$ on the plane $z/a = 0$ for $u'/U = 33\%$; the z-axis points out of the page.

upper pair of curves is the total dissipation and the lower one that due to the mean flow. The difference between these two lines is the fluctuation dissipation. It is seen that this component contributes more than 50% to the total. The results converge away from the sphere axis, where the dissipation is essentially the same as in the particle-free case, but the multi-particle dissipation is always larger than the single-particle one. This is again a manifestation of the greater flow blockage in the former case, due both to the particles and the trailing wakes.

The possibility of a destructive wake-wake interaction, which would give rise to increased dissipation, has been mentioned in the literature.[47] Instantaneous interactions between wakes is evident in many snapshots of the vorticity distribution such as that shown in Figure 19, but it does not seem to play an important role in the configuration and parameter range investigated here perhaps due to the rapid decay of the vortical motions.

A. Hydrodynamic forces

The time history of the normalized streamwise component F_x and cross-stream component F_y of the hydrodynamic force on the central particle in the single and multiple particle simulations are compared in Figures 20(a) and 20(b), where the solid line is the difference between the two. The most noticeable difference is a nearly constant increase of the streamwise component of approximately 19% in the multi-particle case. This value is remarkably close to the value 18%

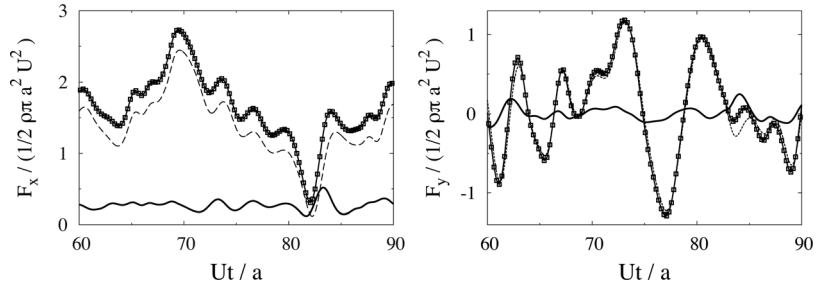

FIG. 20. Time history of the normalized streamwise force F_x and of the cross-stream component F_y of the hydrodynamic force on the central sphere comparing the single (dashed line) and multi-particle (line with symbols) simulations. The solid line is the difference between each force component in the two cases.

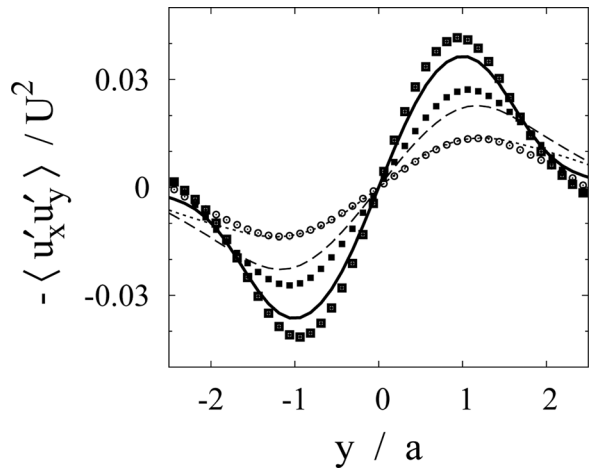

FIG. 21. Reynolds stress along the horizontal line $z = 0$ on cross-stream planes 3, 5, and 7 radii downstream of the sphere for the single- (lines) and multi-particle (symbols) simulations.

obtained from the Schiller-Naumann correlation for the increase in mean velocity of 12% caused by the flow blockage. Other than this feature, the forces in the two cases track each other very closely which implies that the incident turbulence, which is the same for both, is not significantly affected by the neighboring particles.

Generally speaking, when the integral scale is larger than the particle spacing, one may expect the flow field around a particle to be significantly affected by the neighboring particles. This "screen effect"[1] would be expected to limit the largest eddies to a scale comparable to the inter-particle separation. In our case, the incident turbulence scale is not large compared with the inter-particle separation, but the main reason for the lack of interaction is probably the particular planar geometry of the particle arrangement. We have verified this hypothesis in the course of a limited study of two particles aligned in the direction of the incident flow. Those results do not have much bearing on the issue of turbulence dissipation which is the focus of the present study, and, therefore, they will not be described.

B. Reynolds stresses

Figure 21 shows the Reynolds stress $-\langle u_x' u_y' \rangle / U^2$ along the horizontal line $z = 0$ on cross-stream planes 3, 5 and 7 radii downstream of the sphere. The lines and symbols are for the single- and multi-particle simulations, respectively. The numerical values and trends of these results are comparable with those reported in Ref. 10.

In the multi-particle case the stronger mean-velocity gradients due to the flow blockage increase the turbulence production and the Reynolds stress is therefore greater than for the single-particle case, although the difference decreases with downstream distance. The multi-particle stress is close to zero at the edges of the diagram due to the quasi-periodicity enforced by the presence of the other particles.

The derivative $\partial \langle u_x \rangle / \partial y$ of the mean velocity, which we do not show for brevity, behaves very much in the same way as $-\langle u_x' u_y' \rangle / U^2$ which suggests the appropriateness of a description in terms of a turbulent viscosity. Therefore, in a non-decaying turbulent flow, one would expect a faster broadening of the peak and trough of the curves shown in Figure 21 due to the increased turbulent viscosity and a slower decay of the maxima and minima with distance.

VII. CONCLUSIONS

We have studied the interaction between fixed spherical particles and homogeneous isotropic turbulence convected past them. We have considered a single sphere and nine spheres arranged regularly in a plane lattice perpendicular to the mean flow direction. The size of the particles is

larger than the Kolmogorov scale and comparable to the Taylor micro-scale. The turbulence intensities simulated were relatively large, $u'/U = 17\%$ and 33%.

In our parameter range, most of the dissipation induced by a particle occurs in the neighborhood of its surface, i.e., in the boundary layer region and in the potential region ahead of the mean stagnation point (Figures 3 and 5). Dissipation in the wake was found to be comparatively less important, in particular for the larger turbulence case. With increasing turbulence, the mean-flow dissipation in the wake is reduced (Figure 6) and the turbulent dissipation recovers the particle-free value faster (Figure 8).

Estimating the turbulent dissipation from the force on the particle captures the order of magnitude of the average fluctuating dissipation (Figure 9), but instantaneously can be in error by a large amount (Figure 10). Unsteady flow phenomena occurring in the wake, for instance, the stimulated shedding of vorticity illustrated in Figure 16, and in the immediate neighborhood of the particle surface, play a significant role in explaining this discrepancy.

The simulation in which nine particles are arranged in a planar lattice normal to the mean flow reveals that the particle-induced dissipation does not scale linearly with the number of particles (Figure 17). The main mechanism responsible for this feature is the increased flow blockage which leads to an increase of the mean flow velocity near the particles. The fluctuating hydrodynamic force on the particles is little affected by the blockage, which only increases the mean value (Figure 20) to an extent comparable with that predicted by standard drag correlations. The Reynolds stress (Figure 21) and the turbulence production are also increased.

An obvious next step in a study of this type is to allow the particles to move, which is quite possible with the numerical method that we have used.

ACKNOWLEDGMENTS

This study was supported by the National Science Foundation under Grant Nos. CBET-0625138 and CBET-0754344.

[1]W. Hwang and J. K. Eaton, "Homogeneous and isotropic turbulence modulation by small heavy (St ∼ 50) particles," J. Fluid Mech. **564**, 361 (2006).
[2]A. Ferrante and S. Elghobashi, "On the physical mechanism of two-way coupling in particle laden isotropic turbulence," Phys. Fluids **15**, 315 (2003).
[3]S. Elghobashi, "An updated classification map of particle-laden flows," in *Proceedings of the IUTAM Symposium on Computational Multiphase Flow*, Fluid Mechanics and its Applications (Springer, New York, 2006), Vol. 81, pp. 3–10.
[4]S. Sundaram and L. R. Collins, "Collision statistics in an isotropic particle-laden turbulent suspension. Part 1. Direct numerical simulations," J. Fluid Mech. **335**, 75 (1997).
[5]L. I. Zaichik, O. Simonin, and V. M. Alipchenkov, "Collision rates of bidisperse inertial particles in isotropic turbulence," Phys. Fluids **18**, 035110 (2006).
[6]K. D. Squires and J. K. Eaton, "Preferential concentration of particles by turbulence," Phys. Fluids **3**, 1169 (1991).
[7]J. Bec, "Fractal clustering of inertial particles in random flows," Phys. Fluids **15**, L81 (2003).
[8]R. A. Gore and C. T. Crowe, "Effect of particle size on modulating turbulent intensity," Int. J. Multiphase Flow **15**, 279 (1989).
[9]T. M. Burton and J. K. Eaton, "Fully resolved simulations of particle-turbulence interaction," J. Fluid Mech. **545**, 67 (2005).
[10]Z. Amoura, V. Roig, F. Risso, and A.-M. Billet, "Attenuation of the wake of a sphere in an intense incident turbulence with large length scales," Phys. Fluids **22**, 055105 (2010).
[11]A. Naso and A. Prosperetti, "The interaction between a solid particle and a turbulent flow," New J. Phys. **12**, 033040 (2010).
[12]J. M. Yusof, "Interaction of massive particles with turbulence," Ph.D. thesis (Cornell University, 1996).
[13]P. Bagchi and S. Balachandar, "Response of the wake of an isolated particle to an isotropic turbulent flow," J. Fluid Mech. **518**, 95 (2004).
[14]J.-S. Wu and G. M. Faeth, "Sphere wakes at moderate Reynolds numbers in a turbulent environment," AIAA J. **32**, 535 (1994).
[15]J.-S. Wu and G. M. Faeth, "Effect of ambient turbulence intensity on sphere wakes at intermediate Reynolds numbers," AIAA J. **33**, 171 (1994).
[16]S. Pope, *Turbulent Flows* (Cambridge University Press, Cambridge, UK, 2000).
[17]M. S. Uberoi and P. Freymuth, "Turbulent energy balance and spectra of the axisymmetric wake," Phys. Fluids **13**, 2205 (1970).
[18]J.-H. Chen, "Turbulence generation in homogeneous dilute particle-laden flows," Ph.D. thesis (University of Michigan, 1999).
[19]P. Bagchi, "Particle dynamics in inhomogeneous flows at moderate-to-high Reynolds number," Ph.D. thesis (University of Illinois, Urbana, IL, 2002).
[20]A. ten Cate, J. J. Derksen, L. M. Portela, and H. E. A. van den Akker, "Fully resolved simulations of colliding monodisperse spheres in forced isotropic turbulence," J. Fluid Mech. **519**, 233 (2004).

[21]M. Uhlmann, "Interface-resolved direct numerical simulation of vertical particulate channel flow in the turbulent regime," Phys. Fluids **20**, 053305 (2008).
[22]F. Lucci, A. Ferrante, and S. Elghobashi, "Modulation of isotropic turbulence by particles of Taylor length-scale size," J. Fluid Mech. **650**, 5 (2010).
[23]S. Takagi, H. Z. Z. Oguz, and A. Prosperetti, "PHYSALIS: a new method for particle simulations. Part II: Two-dimensional Navier-Stokes flow around cylinders," J. Comput. Phys. **187**(2), 371 (2003).
[24]Z. Zhang and A. Prosperetti, "A method for particle simulation," J. Appl. Mech. **70**, 64 (2003).
[25]Z. Zhang and A. Prosperetti, "A second-order method for three-dimensional particle simulation," J. Comput. Phys. **210**, 292 (2005).
[26]H. Lamb, *Hydrodynamics*, 6th ed. (Cambridge University Press, Cambridge, UK, 1993).
[27]S. Kim and S. J. Karrila, *Microhydrodynamics: Principles and Selected Applications* (Dover, New York, 2005).
[28]Z. Zhang, L. Botto, and A. Prosperetti, "Microstructural effects in a fully resolved simulation of 1024 sedimenting spheres," in *IUTAM Symposium on Computational Approaches to Multiphase Flow*, Fluid Mechanics and its Applications, Vol. 81, The Netherlands (Springer, 2006).
[29]J. J. Bluemink, D. Lohse, A. Prosperetti, and L. Van Wijngaarden, "A sphere in a uniformly rotating or shearing flow," J. Fluid Mech. **600**, 201 (2008).
[30]L. Botto, "Numerical simulation of extended particles in a fluid flow," Ph.D. thesis (Johns Hopkins University, 2009).
[31]S. Lundgren, "Linearly forced isotropic turbulence," Annual Research Briefs. Technical report, Center for Turbulence Research, Stanford University, 2003.
[32]C. Rosales and C. Meneveau, "Linear forcing in numerical simulations of isotropic turbulence: Physical space implementations and convergence properties," Phys. Fluids **17**, 095106 (2005).
[33]P. Bagchi and S. Balachandar, "Effect of turbulence on the drag and lift of a particle," Phys. Fluids **15**, 3496 (2003).
[34]R. N. Parthasarathy and G. M. Faeth, "Turbulence modulation in homogeneous dilute particle-laden flows," J. Fluid Mech. **220**, 485 (1990).
[35]J. D. Kulick, J. R. Fessler, and J. K. Eaton, "Particle response and turbulence modification in fully developed channel flow," J. Fluid Mech. **277**, 109 (1994).
[36]Y. Sato and K. Hishida, "Transport process of turbulent energy in particle-laden turbulent flow," Int. J. Heat Fluid Flow **17**(3), 202 (1996).
[37]C. Poelma, J. Westerweel, and G. Ooms, "Particle-fluid interactions in grid-generated turbulence," J. Fluid Mech. **589**, 315 (2007).
[38]R. Natarajan and A. Acrivos, "The instability of the steady flow past spheres and disks," J. Fluid Mech. **254**, 323 (1993).
[39]*Computational Methods in Multiphase Flow*, edited by A. Prosperetti and G. Tryggvason (Cambridge University Press, Cambridge, UK, 2009), paperback edition.
[40]D. Legendre, A. Merle, and J. Magnaudet, "Wake of a spherical bubble or a solid sphere set fixed in a turbulent environment," Phys. Fluids **18**, 048102 (2006).
[41]G. K. Batchelor, *An Introduction to Fluid Mechanics* (Cambridge University Press, Cambridge, UK, 1967).
[42]L. D. Landau and E. M. Lifshitz, *Fluid Mechanics* (Pergamon, London, UK, 1987).
[43]K. T. Kiger and J. C. Lasheras, "Dissipation due to particle/turbulence interaction in a two-phase, turbulent, shear layer," Phys. Fluids **9**, 3005 (1997).
[44]R. Mittal, "Response of the sphere wake to freestream fluctuations," Theor. Comput. Fluid Dyn. **13**, 397 (2000).
[45]B. Ghidersa and J. Dusek, "Breaking of axisymmetry and onset of unsteadiness in the wake of a sphere," J. Fluid Mech. **423**, 33 (2000).
[46]M. Jenny, J. Dusek, and G. Bouchet, "Instabilities and transition of a sphere falling or ascending freely in a Newtonian fluid," J. Fluid Mech. **508**, 201 (2004).
[47]J. C. R. Hunt and I. Eames, "The disappearance of laminar and turbulent wakes in complex flows," J. Fluid. Mech. **457**, 111 (2002).